Combustion and Flame 284 (2026) 114631

Contents lists available at ScienceDirect

Combustion and Flame

journal homepage: www.sciencedirect.com/journal/combustion-and-flame

Soot and nanoparticle formation in ethylene counterflow diffusion flames: effects of nitrogen dilution and strain rate

Vincenzo Esposito [a,*], Alberto Cuoci [b], Alessandro Stagni [b], Alessio Frassoldati [b], Mariano Sirignano [a]

[a] Università Degli Studi di Napoli Federico II, Dipartimento di Ingegneria Chimica, Dei Materiali e Della Produzione Industriale, P.le V. Tecchio, 80, Napoli 80125, Italy
[b] CRECK Modeling Lab, Department of Chemistry, Materials, and Chemical Engineering – Politecnico di Milano, Piazza Leonardo da Vinci 32, Milano 20133, Italy

ARTICLE INFO

Keywords:
ethylene counterflow diffusion flame
soot
dilution
strain rate
flame structure

ABSTRACT

Stricter health regulations now cap sub-23 nm particle emissions from all combustion devices. High strain rate (α) and inert dilution each curb soot formation. To our knowledge, however, their combined effect on nanoparticle inception and soot growth has never been quantified in a single, well-characterised burner.

To decouple these effects, we systematically investigated ethylene (C_2H_4) counterflow diffusion flames (CDFs) at three nitrogen (N_2)-dilution levels (baseline SF21, and the more heavily diluted SF26 and SF18) while changing the α from 26 to 103 s^{-1}. Dual-wavelength laser induced fluorescence UV-LIF (at 350 nm) and laser induced incandescence LII (at 500 nm) yielded spatially resolved nanoparticle and soot maps. Across all dilutions, increasing the α from 26 to 103 s^{-1} lowered the peak soot-volume fraction (SVF) by 78–82 % and reduced the maximum LII signal proportionally, confirming the sensitivity of soot growth to the residence time. Nanoparticle LIF behaved asymmetrically: in the fuel-rich (pyrolytic) zone, it fell by ≈ 30 %, whereas on the oxidizer side, it plunged by ≈ 62 %. At the same time, the axial location of the maximum rate of soot formation advanced about 1.0 ± 0.1 mm toward the stagnation plane (SP), and sectional modelling reproduced this shift within 15 %. Dilution amplified the strain-induced attenuation, especially in the oxidative zone, but alone could not match the reduction achieved at the highest α. Moderate N_2 dilution combined with high α clarifies how reduced residence time and enhanced mixing jointly suppress nanoparticle inception and soot growth. Importantly, this approach does so without changing the fuel composition or compromising flame stability.

1. Introduction

Hydrocarbon fuels are still widely used in industry and transportation [1], but their combustion often generates particulate matter (PM) emissions. Soot formation during combustion has well-documented adverse effects on both the environment and human health. Specifically, fine particles with diameters of 10 μm or less (PM10) can be retained in the respiratory tract. In particular, ultrafine particles (PM2.5) can penetrate deeply into the pulmonary system and enter the bloodstream, posing serious risks of cardiovascular and respiratory diseases [2–4]. Moreover, these particles contribute to global warming [3,4] and negatively impact both aquatic and terrestrial ecosystems. As reported by Hansen and Nazarenko [4], soot's climate-forcing potential is nearly double that of CO_2, prompting increasingly stringent emission regulations. In fact, to mitigate these issues, regulatory frameworks are establishing increasingly standards for particle emissions in the automotive sector. Notably, the upcoming Euro 7 regulations, effective starting from July 2025, will lower the particle size threshold for measurement from 23 nm (as defined by Euro 6) to 10 nm [5,6]. Similarly, the Environmental Protection Agency (EPA) is projected to implement new regulations for light-duty vehicles (LDVs) in 2027, which include reducing particulate mass emission limits from 3 mg/mi to 0.5 mg/mi [7]. Accordingly, a deeper grasp of the physicochemical pathways leading from gas-phase precursors to solid soot is pivotal for developing next-generation clean-combustion strategies. Soot formation is a multifaceted, kinetics-driven process influenced by fuel structure, dilution, flame temperature, and pressure. Soot evolution is primarily controlled by the flow-time scale; counterflow diffusion flames (CDFs), parameterised by the global strain rate (α) [8], are a proven laboratory tool for probing that scale. Higher α reduce soot formation by decreasing residence time. Because the two opposed streams can be tuned independently, CDFs decouple particle growth and

* Corresponding author.
E-mail address: vincenzo.esposito9@unina.it (V. Esposito).

https://doi.org/10.1016/j.combustflame.2025.114631
Received 12 July 2025; Received in revised form 6 November 2025; Accepted 11 November 2025
Available online 20 November 2025

oxidation, giving two canonical setups: Soot-Formation (SF) and Soot-Formation-Oxidation (SFO). In SF flames [8–27], the flame front lies in the oxidative zone near the stagnation plane (SP), with particles convected toward the SP without complete oxidation. Oxidation proceeds via hydroxyl (OH) radicals and competes continuously with particle growth. Two key zones contribute to soot formation: the pyrolytic zone (fuel nozzle to SP) and the oxidative zone (SP to oxidizer nozzle) [23,24,27] . In SFO flames, the flame front is in the pyrolytic zone, where particles are transported to the flame front and oxidized by molecular oxygen (O_2) similar to co-flow flames. Studying the impact of α [6,8,10,11,19,26] on particle formation is essential to advancing our understanding of soot kinetics and for developing practical flamelet models that account for transient effects [29]. As discussed by Wang and Chung [10], increasing α reduces soot formation by decreasing residence time, polycyclic aromatic hydrocarbons (PAHs) concentration, soot inception rate, and soot surface growth rate per unit volume. Extensive research has been conducted on soot formation in flames fueled by alkanes [16,18,21], ethylene (C_2H_4) [9,13,15,18,20,28,30] and complex fuels, including surrogates [14,31], using CDFs. These studies have demonstrated the beneficial effect of α in mitigating soot formation, offering valuable insights for soot modelling in practical combustion devices. Quadarella et al. [32] proposed a consistent nucleation model and validated α sensitivity using existing SF flames datasets. These flames had a near-fixed stoichiometric mixture fraction (ξ_{st}) of about 0.07-0.075, and were analyzed by varying α, without performing a systematic sweep of ξ_{st} at fixed fuel and oxidizer supply conditions. Moreover, another effective technique for studying soot formation in diffusion flames is the addition of inert gases [33,34]. This approach alters both the flame temperature and the concentrations of reactive species in the streams, depending on whether dilution is applied to one or both sides. The significance of fuel dilution on soot formation was first explored by Glassman and colleagues [35,36]. Specifically, Glassman and Yaccarino [35] introduced monoatomic and diatomic inert gases (Argon (Ar) and N_2, respectively) into a coflow flame and observed that, for the same adiabatic flame temperature (T_{AD}), the argon-diluted flame exhibited a lower tendency to form soot. Since a higher concentration of Ar is required than N_2 to maintain the same T_{AD}, the reduced soot formation suggests that lowering fuel concentration effectively reduces soot production. However, as the observed differences in soot height were deemed small compared to those caused by changes in flame temperature, it was suggested that the effect of fuel partial pressure is secondary to temperature. Kent and Wagner [34] later demonstrated that soot reduction from fuel dilution surpasses what a mere temperature decrease can explain, highlighting the pivotal role of fuel concentration in soot production. Their findings emphasized the pivotal role of fuel concentration in soot production, demonstrating that the effects of fuel dilution cannot be reduced to a mere temperature dependence. Dilution was also used by Sarnacki and Chelliah [37] to investigate pressure effects up to 30 atm, to maintain laminarity and identify sooting limits. Consequently, ξ_{st} decreased and was not considered as the primary parameter under fixed fuel and oxidizer flow conditions. Mechanistically, adding inerts lowers flame temperature and simultaneously reduces fuel concentration, thereby decreasing soot inception and surface growth rates. Similar concerns arise when the flame temperature is adjusted by varying the N_2 content in the oxidizer stream. Changing the ratio of N_2 to O_2 affects the O_2 penetration across the flame into the fuel side. Since small amounts of O_2 in the fuel stream can promote pyrolysis [36], soot formation may be influenced by the varying levels of O_2 penetration. In this contest, Xu et al. [20] varied O_2 composition to study its non-monotonic effect on soot. In this approach, the resulting changes in fuel/oxidizer flow and in the ξ_{st} were a consequence of the imposed O_2 variation, rather than being independently controlled at fixed fuel and oxidizer supply rates. Finally, Randolph and Law [38] studied soot formation in burning droplets of fuel blends consisting of sooty and non-sooty fuels. They showed that diluting sooty fuels with non-sooty components, even when the fuels have nearly identical adiabatic flame temperature, can significantly reduce soot formation. Building on the aforementioned findings, this work investigates ethylene (C_2H_4) SF-CDFs under varying N_2 dilution conditions (79, 75, 69% by volume in the fuel stream;74, 79, 82% by volume in the oxidizer stream) at α from 26 to 103 s^{-1}. This approach allows for simultaneous investigation of the effects of dilution and α. Specifically, we conducted in-situ spectroscopic diagnostics to investigate both nanoparticle inception and soot formation. In addition, numerical simulations using sectional method were conducted to better understand the combined effect of dilution and α on particle production.

2. Experimental setup

The counterflow burner and diagnostic system were described previously [13,23,24,27,39–46]; here, we summarize only essential details. Gas streams enter through two 2.54 cm-i.d. nozzles—one for oxidizer (upper) and one for fuel (lower)—with velocities calculated at 25 °C and 1 atm, and a fixed separation of 1.5 cm. The resulting α ranges from 26 s^{-1} to 103 s^{-1}, calculated according to [47,48] using the following equation:

$$\alpha = 2\frac{v_o}{L}\left[1+\frac{v_f}{v_o}\sqrt{\frac{\rho_f}{\rho_o}}\right] \quad (1)$$

where v_f, v_o, ρ_f, ρ_o and L represent the fuel outlet velocity, oxidizer outlet velocity, fuel density, oxidizer density, and the separation distance of the opposite jets, respectively. Detailed operating conditions are reported in Tables 1 and 2. This Different dilution conditions were established by holding the C_2H_4 flow rate, O_2 flow rate, and a constant, while varying N_2 content on both the fuel and oxidizer sides and adjusting the corresponding flow velocities. Specifically, three dilution cases (SF26, SF21, and SF18) were designed by starting from a baseline C_2H_4 SF-CDF (SF21: 21% O_2, 25% C_2H_4, balance N_2) previously characterized [13,39,43,49]. This reference flame was selected because the 21% O_2 by volume resembles air composition, while the 25% C_2H_4 by volume has been widely explored [13,39,43,49], providing a direct link to established benchmarks. Furthermore, SF21 yields moderate soot loading, representative of modern combustion environments where soot levels are significantly lower than in traditional flames. Indeed, in SF26 and SF18 the oxidizer contained 26, and 18% O_2 by volume, respectively, while the fuel stream contained 21%, and 31% C_2H_4 by volume. These two dilution conditions (SF26, SF21) were generated by

Table 1
Strain rates and stream compositions (mole fractions) of the investigated flames.

	SF26/ξ_{st} = 0.29		SF21/ξ_{st} = 0.21		SF18/ξ_{st} = 0.15	
	Fuel nozzle	Oxidizer Nozzle	Fuel nozzle	Oxidizer nozzle	Fuel nozzle	Oxidizer nozzle
α	$y_{C_2H_4}$	y_{O_2}	$y_{C_2H_4}$	y_{O_2}	$y_{C_2H_4}$	y_{O_2}
[s^{-1}]	[-]	[-]	[-]	[-]	[-]	[-]
26 ± 1	0.21	0.26	0.25	0.21	0.31	0.18
39 ± 1	0.21	0.26	0.25	0.21	0.31	0.18
52 ± 1	0.21	0.26	0.25	0.21	0.31	0.18
103 ± 1	0.21	0.26	0.25	0.21	0.31	0.18

Table 2
Strain rates and nozzle-exit velocities of the investigated flames.

	SF26/ξ_{st} = 0.29		SF21/ξ_{st} = 0.21		SF18/ξ_{st} = 0.15	
	Fuel nozzle	Oxidizer Nozzle	Fuel nozzle	Oxidizer nozzle	Fuel nozzle	Oxidizer nozzle
α	$v_{C_2H_4+N_2}$	$v_{O_2+N_2}$	$v_{C_2H_4+N_2}$	$v_{O_2+N_2}$	$v_{C_2H_4+N_2}$	$v_{O_2+N_2}$
[s^{-1}]	[cm/s]	[cm/s]	[cm/s]	[cm/s]	[cm/s]	[cm/s]
26 ± 1	11.98	8.03	10	10	8.03	11.98
39 ± 1	17.96	12.04	15	15	12.04	17.96
52 ± 1	23.95	16.05	20	20	16.05	23.95
103 ± 1	47.90	32.10	40	40	32.10	47.90

redistributing the amount of N_2 between the fuel and oxidizer sides, while keeping the absolute C_2H_4 and O_2 flow rates fixed. Thus, when O_2 was reduced from 26% to 18% by volume, C_2H_4 correspondingly changes in the fuel side from 21% to 31% by volume, with the balance made up by N_2. This design ensures that the total and the oxidizer molar inputs remain constant, and only the inert dilution is varied. In this way, it is possible to isolate the influence of N_2 dilution on temperature, residence time, and soot formation without changing the global fuel/oxidizer supply or the nominal α. This approach, in terms of redistribution of N_2 amount between the fuel and the oxidizer sides, can be better understood by examining Table 2, which reports the exit-nozzle velocities. Particularly, SF26 and SF18 exhibit the same velocities values, with the roles of the fuel and oxidizer sides reversed. Based on these three dilution conditions (SF26, SF21, and SF18), the flames can also be characterized by calculating their respective stoichiometric mixture fraction (ξ_{st}). In general, the mixture fraction can be calculated as:

$$Z = \frac{\sum\left[N_{C,i} \times Y_i \times \left(\frac{M_C}{M_i}\right)\right]}{+\sum\left[N_{H,i} \times Y_i \times \left(\frac{M_H}{M_i}\right)\right]} \quad (2)$$

where N_C and N_H represents the number of carbon (C) and hydrogen (H) atoms in species i, Y_i is the mass fractions of the species, while M_C and M_H are the molecular weight of C and H atoms, respectively. Then, Z can be normalized as:

$$\xi = \frac{Z - Z_o}{Z_f - Z_o} \quad (3)$$

where subscripts f and o correspond to fuel and oxidizer streams. Using only the mass fraction of fuel and oxidizer under stoichiometric proportions ξ_{st} can be calculated as follow:

$$\xi_{st} = \left[1 + \left(\frac{Y_f M_o \nu_o}{Y_o M_f \nu_f}\right)\right]^{-1} \quad (4)$$

Once again, Y_f, Y_o, M_f, M_o are the mass fraction and the molecular weight of fuel and oxygen respectively, whereas ν_f and ν_o are their stoichiometric coefficients. Because the ξ_{st} depends on the inlet mass fractions, ξ does vary slightly between the three flames. The burner is thermoregulated with a circulating system maintained at 80°C, and the fuel stream is electrically preheated to 150°C. As a result, the exit temperatures were measured as 80 °C for the oxidizer nozzle and 115 °C for the fuel nozzle. This burner configuration with screened and thermoregulated nozzles ensures uniform exit conditions. Flow-straightening screens provide nearly plug-like profiles (deviation < 5%), while the aspect ratio (D/L ≈ 1.7) lies within the recommended design range for CDFs [50]. The opposed jet interaction further flattens the velocity field. These features minimize radial gradients and confirm that this geometry produces a proper CDF, unaffected by boundary artefacts. For spectrally and spatially resolved Laser-Induced Emission (LIE) measurements in the 200–500 nm range, we employed a pulsed Nd:YAG laser running at its fourth harmonic (266 nm). The laser energy was maintained at 0.8 mJ with a pulse duration of 8 ns and a repetition rate of 10 Hz. The laser beam, with a diameter of 250 μm at the focal point — corresponding to an irradiance of 1.6 J/cm² — was exactly focused on the flame center. This beam size is comparable to that employed in previous studies [13,23–25,39,41–43,51,52]. Given the beam dimensions and the flame thickness, particularly at the highest strain rates, signal convolution and profile smoothing cannot be ruled out and should be considered in future model comparisons. In particular, the main source of uncertainty in LIE measurements stems from this beam dimension relative to the typical thickness of the particle-laden region (ca. 1-2 mm), which decreases at higher α. As a result, the collected signal represents a spatial convolution of the emission within the beam volume. This effect is most pronounced at the highest α, where soot or nanoparticle-containing region becomes very thin. In these cases, the convolution tends to produce smoother, broadened profiles and can lead to a slight underestimation of the peak signal intensity. Based on optical setup and calibration (detection optics, gate width, and beam alignment), it has been estimated to have an uncertainty of approximately ± 5-10% in peak signal intensity and spatial resolution of ca. 0.3 mm. Conversely, the uncertainty in the inferred axial position of the signal peak is smaller (± 0.2 mm). These values are consistent with prior works of similar diagnostics in CDFs [24,44]. The emitted radiation was directed through a 280 μm entrance slit of a spectrometer and recorded using an intensified CCD camera, thermoelectrically cooled to −10°C to minimize noise. The detection system was positioned at 90° relative to the laser beam. Emission spectra, Laser-Induced Fluorescence (LIF), and Laser-Induced Incandescence (LII) signals were acquired using a 100 ns gate time synchronized with the laser pulse, and by averaging the CCD signal over 150 laser scans. Scattering at 266 nm (Qvv@266 nm) was also measured, using double vertical polarization (Qvv) to eliminate angular dependence. Each measurement was repeated at least five times, and the reported values in the figures represent the mean, with error bars indicating the variance. The simultaneous deployment of LIF, LII, and Qvv@266 nm in the same flames, allowing us to separate nanoparticle inception (LIF) from soot mass (LII), and to locate the particle stagnation region. In this way, it is possible to capture the differing behaviors of LIF and LII signals – reflecting nanoparticles versus soot mass – that would be difficult to identify with fewer measurements. Instead, prior CDFs studies typically used one or two diagnostics (e.g., extinction or LII) [20,32,37]. The entire burner assembly was mounted on a translation stage with a spatial resolution of 0.1 mm, allowing vertical movement relative to the measurement point. This enabled spatially resolved measurements across the flame, from the fuel to the oxidizer side, providing a detailed characterization of nanoparticle and soot formation and evolution in the flame. LIF and LII signals are simultaneously detected in flames, revealing two distinct fluorescence maxima, whose characteristics depend on flame structure and operating conditions [23,24,44,46]. The first maximum, located in the near-UV region, was prominent in both premixed and counterflow diffusion flames. The second, centered around 400 nm, was more evident in premixed flames with high equivalence ratios and in the fuel-rich regions of diffusion flames. Previous studies have attributed near-UV fluorescence to nascent nanoparticles composed of small polycyclic aromatic hydrocarbons (PAHs) containing 2–3 aromatic rings, whereas

the visible fluorescence was associated with the aromatization of PAH precursors during their transformation into soot nuclei [23,24,44,46]. Spatially resolved spectroscopic measurements in CDFs further correlated visible fluorescence in the fuel zone with the presence of densely packed PAH clusters. The LII signal, observed as a broadband visible continuum, is ascribed to thermal emission from solid soot particles. Under heavily sooting conditions, a blackbody radiation curve at 3500 K was used to correct LIF profiles and mitigate the interference from long-lived visible emission on fluorescence detection. The soot volume fraction was also derived from the incandescence signal, calibrated using the signal measured in a reference yellow-orange sooting flame doped with 22% oxygen (SF22), which has been extensively characterized in prior studies [23,25]. Temperature measurements were performed with a type-R Pt/Pt-Rh 13% thermocouple and a method previously validated in CDFs [39]. Radiation corrections and conduction losses were applied following standard procedures [53], accounting for bead radiation and gas-bead heat exchange. As a result, there is an uncertainty of ±30-50 K in the peak flame region, which is larger at higher α due to the narrower reaction zones and higher velocities. Bead size (ca. 250 μm) defines spatial resolution, and combined with the heat-exchange boundary layer, it gives a positional uncertainty of ±0.2 mm.

3. Numerical modeling

3.1. Kinetic mechanism and soot modeling

The soot model used in this work is based on a detailed discrete sectional method (DSM), which discretizes heavy PAHs and soot particles into 25 lumped pseudo-species (BINs), ranging from 20 to over 10^8 C atoms, described in [54]. These BINs are spaced by a factor of two between adjacent sections. The early BINs (BIN1–4) represent large PAHs, while BIN5, corresponding to a particle diameter $D_p = 2.02$ *nm* and containing 320 C atoms, is selected as the smallest soot particle. The selection of BIN5 is supported by LII measurements in low-sooting premixed flames [55]. Particles from BIN5 to BIN12 are modeled as spheres, with BIN12 ($D_p = 10.11$ *nm* and 4×10^4 C atoms) serving as the primary particle, forming the building blocks of soot aggregates. These aggregates are modeled with a fractal dimension of 1.8, consistent with observations in premixed C_2H4 flames [56]. This mode assumes a constant primary particle size, thereby neglecting the polydispersity of soot aggregates. Although this simplification enhances computational efficiency, it reduces the accuracy of surface area and diffusion property predictions. A parametric analysis, presented in [54], indicates minimal variations in predicted soot volume fractions (SVF) when the primary particle size varies between BIN9 ($D_p \sim 5$ *nm*) and BIN15 ($D_p \sim 45$ *nm*). To account for the evolution of the hydrogen-to-carbon (H/C) ratio during dehydrogenation and aging, three hydrogenation levels (A, B, C) are assigned to each BIN. The complete soot sub-mechanism consists of 84 pseudo-species and approximately 10,000 reactions categorized into six main reaction classes: soot inception, growth, dehydrogenation, coalescence, aggregation, and oxidation. These classes and their associated rate parameters are reported and discussed in [54,56,57]. A key innovation of this model is the separate treatment of small versus large PAHs, reflecting their different reactive pathways. Up to BIN3 (80 C atoms), PAHs are treated as conventional aromatic molecules, with separate kinetics for closed-shell species and radicals. For larger BINs, particles are treated as persistent radicals, in line with recent theoretical findings indicating that large peri-condensed PAHs behave as open-shell diradicals. This distinction removes the need for activation steps such as H-abstraction in large BINs, simplifying the reaction pathways. The reaction rate constants for small BINs (BIN1–3) are adopted from previous versions of the CRECK soot model [58]. For larger BINs (BIN4–25), rate parameters are defined by analogy to reactions involving resonantly stabilized aromatic radicals. Key reactions include:

1. **Acetylene addition to radicals** ($C_2H_2 + C_7H_7\bullet \rightarrow H\bullet + C_9H_8$), which governs the H abstraction– C addition (HACA) mechanism.
2. **PAH condensation** ($C_6H_6 + C_5H_5\bullet \rightarrow H\bullet + C_{10}H_7CH_3$), describing the growth of PAHs on soot particles.
3. **Oxidation reactions**, incorporating molecular O_2 interactions with benzyl and larger PAHs.

Reactions among BIN4–25 require higher activation energies than BIN1–3, consistent with the strong resonance stabilization of these large radical species. This approach aligns with recent studies and significantly improves predictions of soot oxidation under oxidative environments where abstracting species such as H and OH are scarce [58]. The soot model is integrated with the high-temperature CRECK gas-phase mechanism to simulate the transition from gas-phase species to solid particles. The gas-phase mechanism, available in CHEMKIN format [59], is provided in the Supplementary Material to ensure reproducibility.

3.2. Mathematical and numerical model

All numerical simulations were carried out in the OpenSMOKE++ framework [60] using a one-dimensional laminar flame solver. The solver incorporates mixture-averaged diffusion coefficients, the Soret effect, and particle thermophoresis in the transport equations. The mixture-averaged approximation provides an excellent compromise between accuracy and computational efficiency for CDFs, where differential diffusion effects are moderate. This formulation reliably captures the dominant transport physics without requiring a full multicomponent treatment. The counterflow flame geometry, consisting of two opposing concentric circular nozzles, is assumed to be axisymmetric. Moreover, the following nozzle-exit boundary conditions are employed: C_2H_4/N_2 and O_2/N_2 composition (Table 1), nozzle-exit velocities (Table 2), and inlet temperatures for each flame. Consequently, a emerges self-consistently from the imposed velocities and separation in the 1D counterflow system. The governing conservation equations of mass, momentum, energy, and species are formulated in cylindrical coordinates. The system of equations consists of partial differential equations (PDEs) coupled with algebraic constraints. The equations describe the conservation of mass, momentum, energy, and species, with boundary conditions applied at the nozzles. Details are available in [61]. Fick's law governs the diffusion velocity of chemical species in the gas phase. However, for soot particles (BINs), diffusion is assumed to be dominated by thermophoresis, neglecting interactions with gas-phase species. The diffusion velocity $\boldsymbol{V}_s$ for BIN particles is thus expressed as [62]:

$$\boldsymbol{V}_s = \frac{3}{4\left(1+\frac{\pi\alpha}{8}\right)}\frac{\mu}{\rho T}\nabla T \tag{5}$$

where μ is the dynamic viscosity, ρ is the density, T the temperature, and alpha the thermal accommodation factor (here assumed equal to 0.90). This formulation ensures accurate representation of thermophoretic effects, which play a crucial role in soot transport across high-temperature gradients. The diffusivity of BIN particles is further refined using Stokes' Law with a Cunningham correction to account for slip effects in the transition regime, based on the Knudsen number [63]. This correction is crucial for ensuring accurate modeling of particle dynamics, particularly for the smallest soot particles in the DSM framework. Radiative heat transfer is modeled using the optically thin approximation, which accounts for emissions from major radiating species (H_2O, CO_2, CO, CH_4, and soot). The radiative source term is defined as:

$$Q_{rad} = 4\sigma\left(T^4 - T_{env}^4\right)\left(\sum_i a_i p_i + a_s f_v\right) \tag{6}$$

where a_i is the extinction coefficient for gaseous species i, p_i is the corresponding partial pressure, T_{env} the environmental temperature, and f_v

the soot volume fraction. For soot, the extinction coefficient a_s is computed as:

$$a_s = b_1 \rho_s [1 + b_2 (T - 2000)] \quad (7)$$

where ρ_s is the soot density, the coefficients $b_1 = 1232\ m^2/kg$, and $b_2 = 4.8 \times 10^{-4}\ 1/K$ [64] were obtained by fitting the equation to data based on the Taylor-Foster approximation [65] and data based on the Smith et al. approximation [66]. The units of a_s are m^{-1}. In the present configuration, the optically thin approximation (OTA) is employed due to the very low optical thickness of the counterflow flame ($\tau < 0.05$), resulting from the small characteristic length scale and modest SVF. Under these conditions, reabsorption of emitted radiation is negligible, and the OTA provides an accurate yet computationally efficient estimate of global radiative heat losses. Although soot radiation is included through the semi-empirical formulation of Hall et al. [67], this treatment does not capture spectral variations or morphology-dependent optical properties, which may lead to localized deviations in radiative cooling, particularly in soot-rich regions. Nonetheless, such effects have limited impact on the overall flame structure and energy balance, and the adopted approach is consistent with previous counterflow flame studies [68–71]. Velocity, temperature, and species mass fluxes are prescribed at each nozzle, ensuring an accurate representation of diffusive transport. This method improves system representation compared to directly setting species mass fractions. The governing equations are discretized using finite-difference schemes on a non-uniform grid, with central differencing for diffusion and upwind differencing for convection to enhance stability. The resulting stiff, nonlinear system of equations is solved using the BzzDae solver [72], which leverages the block-tridiagonal structure to ensure computational efficiency and accuracy.

4. Results and discussions

Fig. 1 shows the temperature profiles, both experimental and numerical, for the SF21, SF26, and SF18 ethylene CDFs at different α ranging from 26 s^{-1} to 103 s^{-1}. For both experimental and numerical profiles no empirical shift or alignment was applied. The numerical SP for each flame is also shown in the figure. The combined effects of dilution and α on flame structure can be clearly observed. For all three dilution conditions and across every α, the numerical outcomes broadly match the experimental data. However, some discrepancies beyond the experimental uncertainty are noticeable. As the O_2 content decreases from SF26 to SF18, the peak temperature shifts toward the oxidizer nozzle, where stoichiometric conditions occur. Experimental data show that in SF26, characterized by lower fuel concentration and higher O_2 concentration, the temperature peak is noticeably higher than in the other dilution scenarios. However, the model underestimates this peak, predicting only a smaller rise in temperature. Also, experimental data indicate that the temperature peak position does not significantly shift as α increases. The model is quite able to reproduce this trend although fails to match the peak position, particularly for SF26 flames. Overall, the model exhibits better agreement with experimental data as the O_2 concentration decreases (particularly for SF18 and SF21). Furthermore, the model overestimates peak temperature up to 100 K higher than measured at highest α. This discrepancy can be attributed to the uncertainties in the gas-phase chemistry and transport (i.e., high-

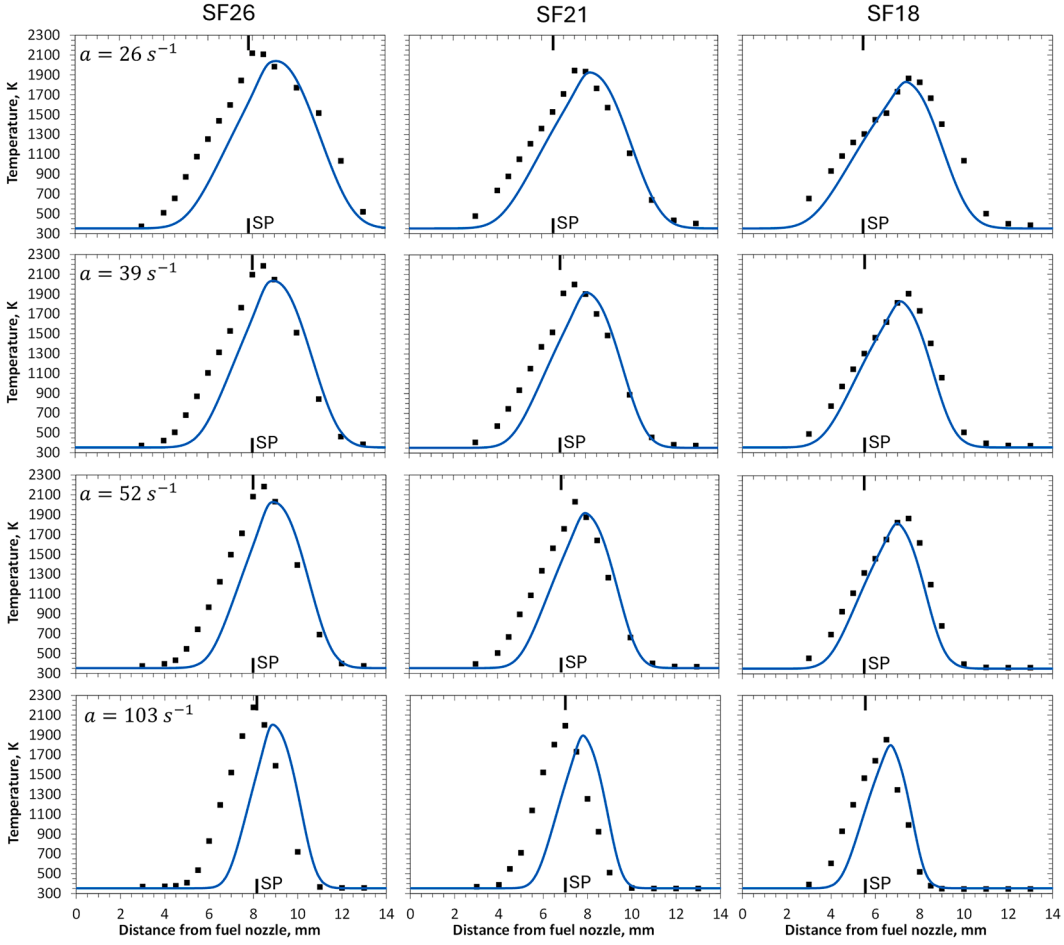

Fig. 1. Experimental (black squares) and numerical (blue lines) temperature profiles in the SF21, SF26, and SF18 counterflow diffusion flames at different strain rates.

temperature kinetics of C_2H_4 oxidation, and radiative heat losses, which are represented in the experiments but only partially in the simulations). In particular, reactions controlling the radical pool, such as $H + O_2 \rightleftharpoons O + OH$ and $H + OH + M \rightleftharpoons H_2O + M$, were found to exert the strongest influence on the computed peak temperature. This behavior is consistent with previous sensitivity analyses of C_2H_4 CDFs [20,32], where variations of ±20 % in the H-recombination rates produced temperature shifts on the order of 50–80 K. Although a full formal sensitivity study was not performed here, the present simulations reproduce comparable trends, supporting the robustness of the adopted mechanism. Also, adiation is dominated by CO_2 and H_2O with soot giving smaller and non-negligible contribution. When the soot loading (≤ few ppm) is reached, soot radiation is expected to lower peak temperature as reported in other studies [20,32]. The already cited uncertainty of ±30-50 K in flame region becomes higher at higher α due to the reduced thickness of the reactive zone and the sharper gradients. Since nucleation and surface growth are strongly temperature dependent, even these moderate discrepancies can have a significant impact on the predicted soot levels. Finally, it should be noted that part of the residual differences between measured and modeled temperature profiles may also reflect experimental uncertainties. Small deviations from ideal flow symmetry or planar flame geometry, as well as uncertainties in mass-flow delivery (≤ 1%) and inlet temperature control (± 50 K), can affect the measured temperature field. Moreover, the thermocouple-based correction relies on heat transfer modeling, whose accuracy depends on bead size, local gas composition, and material properties. These combined effects may contribute to the remaining model–experiment mismatch.

Raising the α shortens the flame length by reducing the residence time. This reduces the efficiency of the chemical reaction and the heat produced, the extreme of this process being the extinction limit. Comparing experimental and numerical results emphasizes the sensitivity of soot modeling to both gas-phase chemistry and heat losses treatment and reveals that dilution has a stronger influence on the temperature than the α does. It is worth noting that the total amounts of fuel, O_2, and diluent are kept constant across all dilution conditions. Likewise, at higher O_2 dilution, the peak temperature shifts into a region with relatively low dilution and thus a locally lower flame temperature than in less-diluted cases. To better understand the impact of different dilution conditions, and to reduce the sensitivity to the absolute positioning of the peak, Fig. 2 reports the experimental and numerical flame temperature peaks against ξ_{st} for SF18, SF21, SF26 ethylene CDFs at different α. It is worth noting that the effect of dilutions becomes more pronounced as α increases, especially between 52 and 103 s^{-1}, where the increase in α is more significant.

Fig. 3 reports the profiles of LIF@350 nm, LII@500 nm, and Qvv@266 nm for the SF18, SF21, and SF26 flames at different α (from 26 s^{-1} to 103 s^{-1}). These three diagnostics respectively detect non-

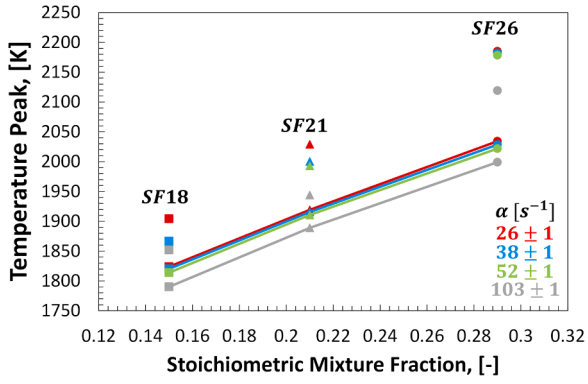

Fig. 2. Experimental (symbols) and numerical (symbols and lines) temperature peak against ξ_{st} for SF18, SF21, SF26 ethylene CDFs at different strain rates.

incandescent nanoparticles (freshly nucleated up to ~5 nm), soot particles (from the smallest incandescent particles to large aggregates), and excess scattering (dominated by condensed-phase species, especially larger ones). Usually, in the experiment SP is identified where the Qvv@266 nm peaks, identifying maximum particle concentration (particles stagnation point), with an uncertainty of ±0.2 mm for all the dilution conditions. In the simulations, the SP is defined by the zero of the axial velocity gradients in the gas-phase stagnation-flow solution. The difference between these two is generally small – in the order of 0.2 mm in line with experimental uncertainty - and mostly due to particle inception and growth that can shift relative to the gas-dynamic SP because of transport, residence-time effects, or oxidation, and the thermophoretic effect that pushes particles in the fuel side. In CDFs, SP has an importance because it marks the region where fuel- and oxidizer-sides transport fluxes are balanced. Thus, it is sensitive to the modeling of diffusion and of the underlaying gas-phase chemistry. Since soot formation processes are strongly coupled to the temperature field, SP also highlights how radiation and transport modeling affect the local structure. In other words, SP emphasize whether the model correctly captures the relative position of the flame with respect to the nozzles, and how the interplay between inception, surface growth, and oxidation evolves under these conditions. Moreover, as α grows, the difference between these two SPs decreases because of stronger convective forces, as reported in Table 3.

Finally, the Qvv@266 nm peak cannot always be identified, due to the very low signal found at higher α. Overall, the pyrolytic and oxidative zones can be identified. These two zones are clearly evidenced in Fig. 4 where numerical profiles of temperature, C_2H_4, O_2, OH for the SF18, SF26, SF21 C_2H_4 CDFs at 39 s^{-1} are reported. The pyrolytic zone fluid-dynamically identified as the zone that extends from the fuel nozzle to gas phase SP is primarily defined by the absence of oxidants, low radical concentrations, and relatively moderate temperatures (up to 1500 K) [13,23–25,39,43,46]. In contrast, the oxidative zone, fluid-dynamically identified as the region from the SP to the oxidizer nozzle, is marked by the presence of the flame front, the high radical concentrations, and the elevated temperatures (up to or exceeding 2000 K).

In the oxidative zone, it is possible to observe the rapid increase of all the signals, indicating the fast nucleation and growth process [13]. Interestingly, and in contrast to many literature reports, the LII@500 nm signal for soot particles remains prominent in the pyrolytic zone. Thus, particles appear in the pyrolytic zone well upstream of the numerically predicted SP, and the LII@500 nm peak is not collocated with the Qvv@266 nm peak. These observations suggest a broader interpretation of particle formation pathways: particles formed in the high-temperature environment rapidly evolve into large aggregates, significantly enhancing the Qvv@266 nm signal. Nevertheless, a substantial fraction of total particle formation occurs in the pyrolytic zone under these conditions. Note that the LII@500 nm signal may be influenced by persistent fluorescence emissions in the visible range. These signals can be significantly enhanced by low temperatures typical of the pyrolytic zone. Nevertheless, the presence of a genuine LII@500 nm signal in the pyrolytic zone cannot be disregarded. As for the impact of dilution, particles are produced in oxidizer side (high temperature environment) in higher amounts as oxidant concentration increases, hence as temperature increases, similarly to coflow flames that exhibit a higher soot formation [73] in O_2-enriched conditions. α strongly affects particle production, with an especially pronounced influence in the pyrolytic zone. Lower temperature present in this zone is more likely to be responsible for an increased sensitivity to a reduction of residence time. Moving from LII@500 nm to LIF@350 nm provides additional insights into particle formation under the investigated conditions. Like LII@500 nm, the LIF@350 nm signal exhibits two distinct behaviors on the fuel and oxidizer sides. In the oxidizer side with high-temperature environment particle formation process follows the usual pathways that can be encountered also in the analysis of the wings of a coflow

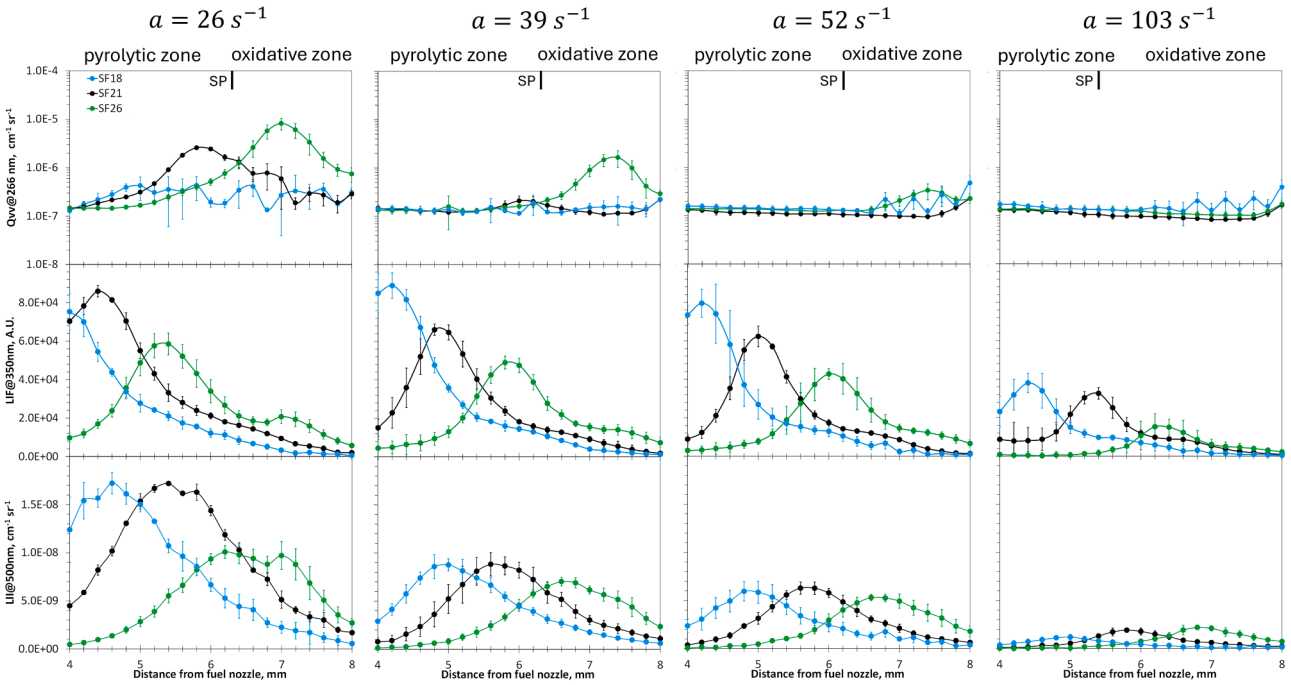

Fig. 3. Scattering (Qvv@266 nm), LIF@350 nm, and LII@500 nm profiles in the SF21, SF26, and SF18 counterflow diffusion flames at different strain rates.

Table 3
Numerical and experimental S.P.

α	SF26/ξ_{st} = 0.29		SF21/ξ_{st} = 0.21		SF18/ξ_{st} = 0.15	
	Exp. S. P.	Num. S. P.	Exp. S. P.	Num. S. P.	Exp S. P.	Num. S. P.
$[s^{-1}]$			[mm]			
26 ± 1	7.0	7.7	5.8	6.6	5.4	5.4
39 ± 1	7.4	7.9	5.9	6.7	5.6	5.5
52 ± 1	7.4	8	6.0	6.8	5.8	5.5
103 ± 1	7.4	8.3	6.0	7.0	6.0	5.6

flame [73]. The higher dilution of the oxidizer stream in SF18 tends to reduce soot formation due to a lower flame temperature. In contrast, LIF@350 nm signals in the pyrolytic zone are predominant in SF18, where the fuel stream contains a higher concentration of C_2H_4 compared to SF26 and SF21. Because the pyrolytic side in SF18 contains more C_2H_4, additional precursors become available for soot, thereby boosting nanoparticle formation. At the lowest α (26 s^{-1}), the two formation processes in the SF26 flame are clearly observable. Starting from the fuel nozzle and progressing toward the SP, LIF@350 nm intensity increases, reaching a maximum. Likewise, the LII@500 nm signal rises shortly after the LIF@350 nm peak, indicating active particle growth. On the other side, starting from the oxidizer nozzle, LIF@350 nm, and LII@500 nm rapidly increase peaking on the same point, also in alignment with Qvv@266 nm. Particles produced on both sides contribute to the total amount of particles produced. The LIF@350 nm signal remains detectable at the highest α, even when the LII@500 nm signal is no longer present. This indicates that nucleation is less sensitive than growth to changes in temperature (and thus residence time). As α increases, the system approaches the extinction limit, leading to a reduction in maximum temperature. This temperature reduction inhibits particle growth, particularly in the oxidative zone, where high radical concentrations and elevated temperatures are essential [8,10,12,15,21]. Fig. 5 shows the normalized LIF@350nm and LII@500nm signals against α for SF26, SF21, SF18 (Fig. S1 in the Supplementary Material shows Fig. 5 with the corresponding error bands). Specifically, the signals are individually normalized to the maximum values detected in the pyrolytic

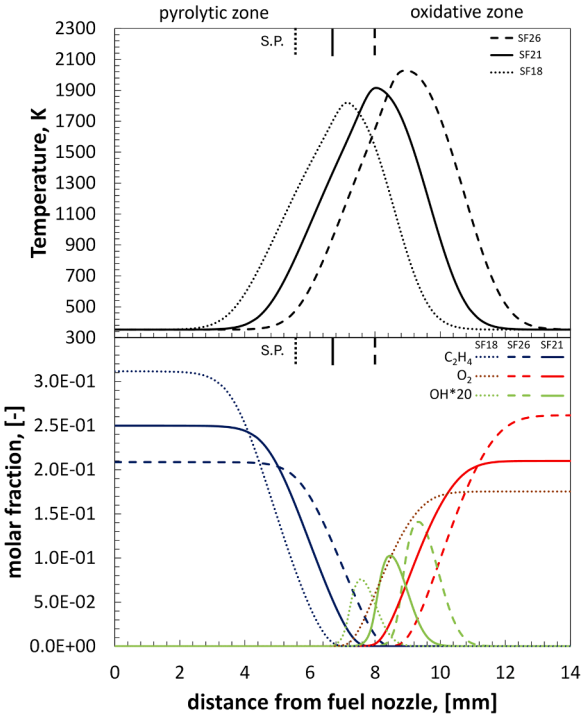

Fig. 4. Numerical profiles of temperature, C_2H_4, O_2, OH for the SF18, SF26, SF21 ethylene CDFs at α = 39 s^{-1}.

and oxidative zone at the lowest α. LIF@350 nm signals normalized to the values detected in the pyrolytic zone, peaks upstream of LII@500 nm and is less affected by dilution showing a ~30% decrease at the highest α.

Conversely, in the oxidative zone, the decrease is approximately 62%. LII@500 nm – tied to soot mass growth – normalized intensity reveals an approximate 80% reduction in signal level across both zones, with the strongest suppression at the highest α. This separation between

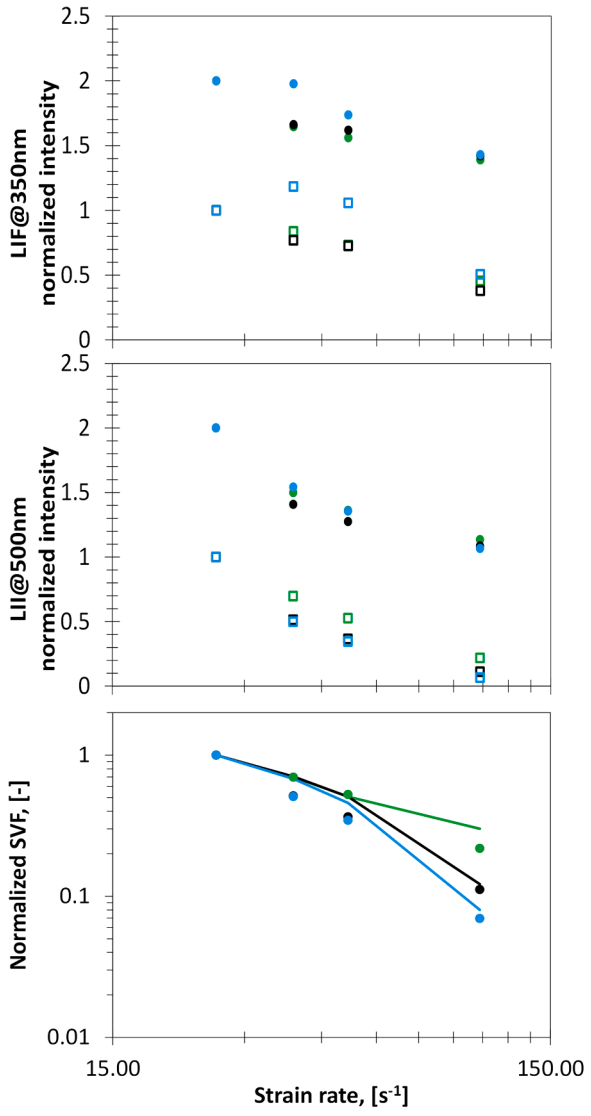

Fig. 5. LIF@350nm, LII@500nm, and soot volume fraction SVF (experimental: full symbols; numerical: solid line) normalized against the strain rate for the three dilution conditions (SF26: green, SF21: black, SF18: light blue). Signals were normalized to the maximum in the pyrolytic zone (full symbols) and the oxidative zone (empty symbols), while both experimental and numerical SVF were normalized to the value at the lowest strain rate.

LIF and LII highlights the difference sensitivities of nucleation and growth processes in the two zones and the important role of the fuel decomposition in the pyrolytic conditions to support particle formation in this zone. Interestingly, the SF26 flame, characterized by a higher peak temperature, exhibits the lowest sensitivity to α. The overall peak of soot volume fraction (SVF) normalized to the value measured at the lowest α for each dilution condition was retrieved from the LII@500 nm signal and reported in Fig. 5. Numerical results were also reported for comparison. This approach clarifies the absolute versus relative influence of α on total particle formation. Soot formation depends on temperature, nucleation, surface growth, and oxidation. Particularly, in this configuration it decreases with increasing α, due to the kinetic control of soot growth. Furthermore, dilution lowers the flame temperature, but at moderate a, the residence times are still long enough for PAH to build up and for nuclei to form on both sides of the stoichiometric surface. Once inception has occurred, growth via HACA is extremely fast, and tends to compensate for the lower peak temperature. For these reasons, soot levels do not decrease in proportion to the temperature drop. At 103 s^{-1}, however, the residence time is much shorter, with less time available for HACA growth and a narrower high-temperature window. Thus, the impact of dilution becomes clearly visible and SVF decreases significantly. Oxidation, mainly by OH, acts on the oxidizer side and determines where the soot zone is truncated, but it does not strongly alter the initial formation stage. Higher oxidant concentrations in SF flames (less dilution) increase SVF by raising temperatures in the pyrolytic zone, which promotes PAH and soot formation. This effect is slightly reduced when the fuel stream is diluted with N_2. Fig. 6 shows the experimental and the numerical SVF for C_2H_4 CDFs at 39 s^{-1}. However, considering that SVF was retrieved from the LII signal, in the pyrolytic zone this latter is significantly contaminated by LIF from nanoparticles and PAH clusters. In many flames LII dominates, but in this configuration, because of the large nanoparticle population and relatively low temperature, LIF contribution is strongly enhanced and biases the apparent SVF. The discrepancy between the experimental and numerical SVF nearly disappears, if the comparison would be restricted to the SP, where the flame temperature is higher and the LII is less affected by LIF. In fact, at this location both the model and the Qvv@266 nm identify the maximum SVF, and the observed trends with decreasing O_2 content are much closer. Thus, interpreting SVF in these conditions requires considering PAH fields together with LII. However, notable discrepancies remain, experimental data show the lowest SVF for SF26, whereas numerical results predict the highest, with a 1 mm shift in SVF peaks between the two.

As an additional examination of how N_2 dilution and α affect the flame, Fig. 7 plots numerical profiles of C_2H_4, O_2, and temperature against ξ for all investigated α, with Z = 0 denoting the oxidizer boundary and Z = 1 the fuel boundary. ξ normalizes such differences and enables direct comparisons. The scope is not to keep ξ exactly constant, but to systematically probe dilution effects under otherwise fixed fuel and oxidizer flow. As the O_2 fraction decreases (SF26 → SF18), the peak flame temperature shifts more noticeably toward the oxidizer side (Z = 0), indicating that dilution has a stronger influence on the maximum temperature than α alone. In the same figure, the mole fractions of C_2H_2,

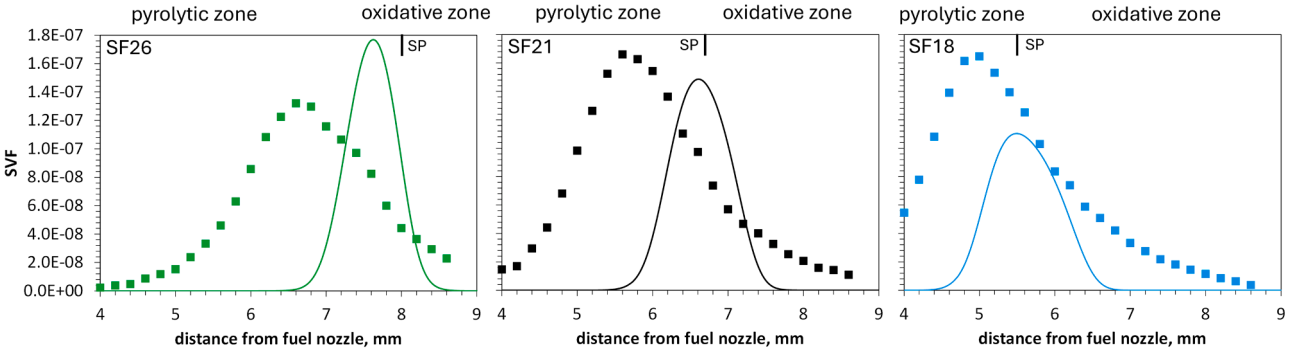

Fig. 6. Experimental (squares) and numerical (solid lines) soot volume fraction profiles for the SF26, SF21, and SF18 ethylene CDFs at α = 39 s^{-1}.

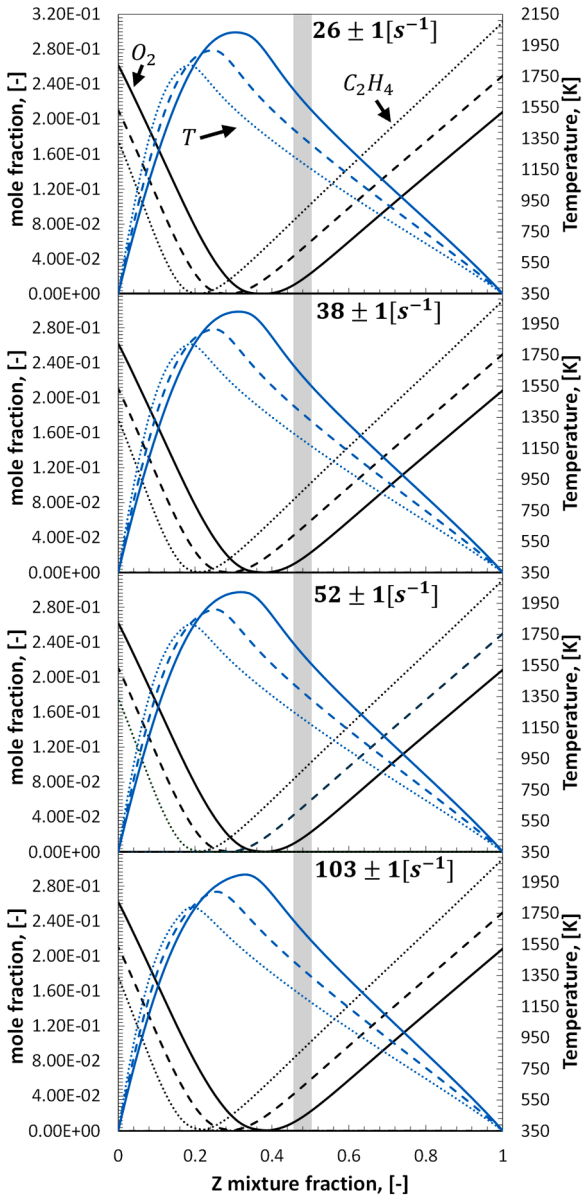

Fig. 7. Numerical profiles of C_2H_4, O_2, and flame temperature in mixture fraction coordinates. Solid lines, dotted lines, and heavily dotted lines indicate SF26, SF21, and SF18, respectively.

A1 (C_6H_6), and A4 ($C_{16}H_{10}$) serve as additional indicators of the soot formation process. Fig. 8 reveals that, at a fixed α, C_2H_2 levels increase from SF26 to SF18, reflecting more effective nucleation, as PAH levels remain high due to resonance-stabilized radicals (RSRs). Notably, A4 remains nearly constant because its formation depends on the combined availability of A1 and C_2H_2, which vary in opposite ways with dilution (A1 increases, C_2H_2 decreases). As a result, A4 remains relatively stable across the three dilutions. Moreover, A1 and A4 increase, most prominently at lower α. From lower to higher α, C_2H_2 shows a slight rise, while A1 and A4 both diminish. These observations highlight the non-monotonic effect of dilution: C_2H_2 is higher in SF26 than in SF18, yet the latter's greater fuel concentration fosters enhanced PAH production and C_2H_2 consumption. The C_2H_2 profiles follow the SVF trends, underlining its central role in HACA-driven surface growth. In line with Fig. 6, SF26 exhibits a larger SVF, underscoring that soot formation depends not just on C_2H_2 but also on factors like flame temperature, nucleation, and growth rates. Taken together, Figs. 6 and 8 emphasize the intricate interplay of PAH and soot formation under these conditions. Although the HACA pathway is widely recognized, recent studies suggest that rapid rearrangements of carbonaceous particles mediated by RSRs also play a significant role in soot chemistry [74]. Finally, as a further investigation of the combined effect of dilution and α, Fig. 9 compares the predicted SVF with the corresponding numerical particle-size distributions (PSDs) for all three dilution levels (SF18, SF21, SF26) over the full range of α. Column (a) plots, for each α, the PSD taken at the axial position where that flame reaches its own SVF maximum. Column (b) shows PSDs extracted at a fixed axial location. This position corresponds to the SVF peak in the highest α case (103 s^{-1}). For the other flames, PSDs are taken at the same distance from the fuel nozzle, as indicated by the dashed line labeled "b". Thus, it shows how the PSD changes with dilution at that common location. All PSDs are normalized to the total particle number in the distribution.

At the lowest α (26 s^{-1}) every flame produces markedly larger particles; the modal diameter shifts toward higher D_p and the tail extends to 100 nanometers (nm). As α rises, the entire distribution contracts. At 103 s^{-1} all three flames are dominated by sub-20 nm particles and the large-particle tail nearly disappears. The drop between 52 s^{-1} and 103 s^{-1} is especially sharp. Among the three dilutions, SF18 still generates slightly smaller particles than SF21 and SF26, hinting that N_2 dilution alone cannot fully compensate for the residence-time penalty imposed by high α. This behavior is somewhat expected since at smaller SVF usually correspond an inhibited growth process and thus also a smaller size. More interestingly, when the SVF is held fixed (at SVF peak of the 103 s^{-1} case which is the lowest), the PSDs reveal a non-trivial trend: regardless of dilution, the highest α yields a larger number of small particles (Dp $\lesssim$ 10 nm) than lower α. Because growth is more sensitive to residence time than inception, most particles remain small. Consequently, SF18, SF21 and SF26 each show a pronounced shoulder in the 5–10 nm range at 103 s^{-1}, whereas at lower α case retains a broader tail of larger particles. These numerical predictions align with the experimental LII and Qvv@266 nm trends in Fig. 3. For a given LII level, the Qvv@266 nm intensity is much weaker at the highest α, implying a smaller average cross-section per particle and hence a finer size distribution. Taken together, the results indicate that the α suppresses growth more effectively than nucleation: higher α leads to many more, but much smaller, particles. N_2 dilution further accentuates this size reduction, but its effect is secondary to the residence-time control exerted by α. This

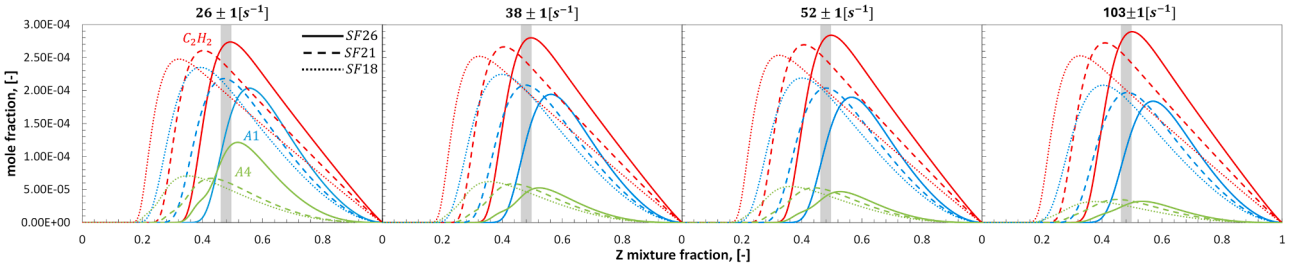

Fig. 8. Numerical profiles of C_2H_2 (red), A1, and A4 mole fractions in mixture fraction coordinates. The grey area represents the zone where the numerical SP is located.

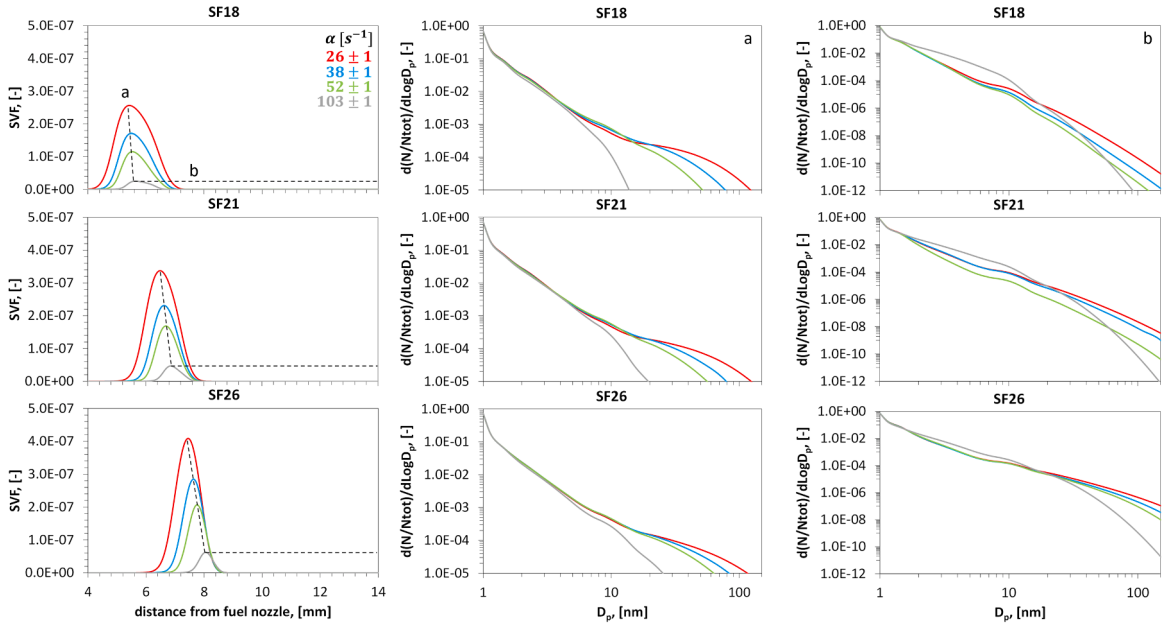

Fig. 9. Numerical Soot Volume Fraction (SVF) (left column) and Particle Size Distributions (PSDs) (column "a" and "b") evaluated for all the dilution conditions (SF18, SF21, SD26) at different strain rates. In column "a", the PSDs are evaluated at the SVF maximum value for each strain rate α, while in column "b", the PSDs are evaluated at the SVF maximum value for SF18, SF21, and SF26 at 103 s^{-1}. Normalization is performed with respect to the total number.

behavior underscores the dual—and partly decoupled—roles of dilution and α: dilution lowers the temperature and slows chemical pathways, whereas α truncates the time available for surface growth. Understanding how these levers independently and jointly shift the PSD provides new insight into tailoring burner conditions to minimize both soot mass and particle size.

5. Conclusions

This study examined soot and nanoparticle formation in ethylene counterflow diffusion flames (CDFs) under varying N_2 dilution and α, using in-situ spectroscopic diagnostics to investigate both the oxidative and pyrolytic zones. The results demonstrate that dilution and α strongly influence flame structure and particle formation. Specifically, N_2 dilution shifts the stoichiometric position and raises the peak flame temperature (which is highest in SF26, the flame with higher O_2 molar fraction in the oxidant stream). In contrast, increasing α primarily reduces particle growth by shortening the residence time and lowering the overall flame temperature. Soot and nanoparticles were observed in both the pyrolytic and oxidative zones. Notably, despite its lower temperatures, the fuel-rich (pyrolytic) zone still produced substantial particles, as indicated by strong LIF and LII signals (particularly in SF26, which has higher C_2H_4 molar fraction in the fuel stream). In contrast, elevated O_2 levels in the oxidative zone promoted rapid soot growth via high-temperature pathways, as evident in simultaneous peaks of LII and scattering. Although α plays a secondary role relative to dilution, its effect is more pronounced in the oxidative zone, where higher temperatures and radical concentrations make particle growth more sensitive to shorter residence times. Quantitatively, the LIF signal in the oxidative zone exhibited a 62% decrease at the highest α, compared to only 30% in the pyrolytic zone, highlighting the resilience of nucleation processes in fuel-rich areas. Meanwhile, LII@500 nm intensities dropped by ~80% across both zones, underscoring the importance of temperature and radicals in particle growth. Flames with higher O_2 content (e.g. SF26) were less sensitive to increased α, likely because their higher peak temperatures still promote soot formation. Conversely, the higher fuel fraction in SF18 supported strong nanoparticle nucleation even at higher α. Overall, these findings broaden our understanding of soot formation in CDFs and offer a clearer picture of how dilution and α can be leveraged to mitigate soot. They underscore the intricate interplay of flame structure, chemical pathways, and flow conditions, providing a foundation for designing cleaner combustion technologies. Future work will expand diagnostic techniques and examine more complex fuels, aiming to further refine kinetic models and extend these insights to practical combustion systems.

Novelty and significance statement

This study provides novel insight into how strain rate (α) and nitrogen (N_2) dilution independently and jointly influence nanoparticle inception and soot growth in diffusion flames approaching extinction. A key innovation is the decoupling of these two effects through a controlled variation of nitrogen dilution in both fuel and oxidizer streams, while keeping ethylene and oxygen flow rates constant. This strategy allows a clear attribution of changes in particle formation to residence time versus dilution effects. The work also demonstrates that nanoparticles, which act as soot precursors, respond differently than larger soot aggregates to these combustion parameters. This distinction underscores the importance of explicitly accounting for nanoparticle dynamics in the modeling and interpretation of soot formation. The findings offer a solid foundation for improving the physical fidelity of predictive models for particulate formation in complex flame environments.

Supplementary material

The manuscript is submitted along with Supplementary Material.

CRediT authorship contribution statement

Vincenzo Esposito: Writing – original draft, Methodology, Data curation, Conceptualization. **Alberto Cuoci:** Writing – original draft, Software, Methodology, Data curation. **Alessandro Stagni:** Writing – original draft, Supervision, Data curation. **Alessio Frassoldati:** Supervision. **Mariano Sirignano:** Writing – original draft, Methodology, Data curation, Conceptualization.

Declaration of competing interest

The authors declare that they have no known competing financial

interests or personal relationships that could have appeared to influence the work reported in this paper.

Acknowledgments

The authors acknowledge funding from: Project funded under the National Recovery and Resilience Plan (NRRP), Mission 4 Component 2 Investment 1.4 - Call for tender No. 3138 of 16 December 2021, rectified by Decree n.3175 of 18 December 2021 of Italian Ministry of University and Research funded by the European Union – NextGenerationEU; Award Number: Project code CN00000033, Concession Decree No. 1034 of 17 June 2022 adopted by the Italian Ministry of University and Research, CUP E63C22000990007 Project title "National Biodiversity Future Center - NBFC" .

Supplementary materials

Supplementary material associated with this article can be found, in the online version, at doi:10.1016/j.combustflame.2025.114631.

References

[1] C. Forsberg, What is the long-term demand for liquid hydrocarbon fuels and feedstocks? Appl. Energy 341 (2023) 121104.
[2] K.C. Kalvakala, V.R. Katta, S.K. Aggarwal, Effects of oxygen-enrichment and fuel unsaturation on soot and NO emissions in ethylene, propane, and propene flames, Combust. Flame 187 (2018) 217–229.
[3] I.M. Kennedy, The health effects of combustion-generated aerosols, Proc. Combust. Inst. 31 (2007) 2757–2770.
[4] J. Hansen, L. Nazarenko, Soot climate forcing via snow and ice albedos, Proc. Natl. Acad. Sci. 101 (2004) 423–428.
[5] R. Abboud, E. Singh, D. Lopez-Pintor, M. Sjöberg, R. Payri, J. López, Effect of operating conditions on soot-formation pathways in an optical direct-injection gasoline engine, Fuel 385 (2025) 134173.
[6] European Commission, Euro 7 standard proposal 2022/0365 (COD), Brussels, 2022.
[7] Environmental Protection Agency (EPA), Multi-Pollutant Emissions Standards for Model Years 2027 and Later Light-Duty and Medium-Duty Vehicles, 2023.
[8] Y. Wang, S.H. Chung, Soot formation in laminar counterflow flames, Prog. Energy Combust. Sci. 74 (2019) 152–238.
[9] H. Böhm, K. Kohse-Höinghaus, F. Lacas, C. Rolon, N. Darabiha, S. Candel, On PAH formation in strained counterflow diffusion flames, Combust. Flame 124 (2001) 127–136.
[10] Y. Wang, S.H. Chung, Strain rate effect on sooting characteristics in laminar counterflow diffusion flames, Combust. Flame 165 (2016) 433–444.
[11] K. Gleason, F. Carbone, A. Gomez, Effect of temperature on soot inception in highly controlled counterflow ethylene diffusion flames, Combust. Flame 192 (2018) 283–294.
[12] V. Huijnen, A.V. Evlampiev, L.M.T. Somers, R.S.G. Baert, L.P.H. de Goey, The effect of the strain rate on PAH/soot formation in laminar counterflow diffusion flames, Combust. Sci. Technol. 182 (2010) 103–123.
[13] V. Esposito, M. Sirignano, Effect of strain rate on nanoparticles and soot in counterflow flames of ethylene/ethanol and ethylene/OME3, Fuel 379 (2025) 133094.
[14] S. Kruse, A. Wick, P. Medwell, A. Attili, J. Beeckmann, H. Pitsch, Experimental and numerical study of soot formation in counterflow diffusion flames of gasoline surrogate components, Combust. Flame 210 (2019) 159–171.
[15] P.H. Joo, Y. Wang, A. Raj, S.H. Chung, Sooting limit in counterflow diffusion flames of ethylene/propane fuels and implication to threshold soot index, Proc. Combust. Inst. 34 (2013) 1803–1809.
[16] K.T. Kang, J.Y. Hwang, S.H. Chung, W. Lee, Soot zone structure and sooting limit in diffusion flames: comparison of counterflow and co-flow flames, Combust. Flame 109 (1997) 266–281.
[17] A. Kalbhor, R. Schmitz, A. Ramirez, P. Vlavakis, F.P. Hagen, F. Ferraro, et al., Experimental and numerical investigation on soot formation and evolution of particle size distribution in laminar counterflow ethylene flames, Combust. Flame 260 (2024) 113220.
[18] L. Xu, F. Yan, Y. Wang, A comparative study of the sooting tendencies of various C5–C8 alkanes, alkenes and cycloalkanes in counterflow diffusion flames, Appl. Energy Combust. Sci. 1–4 (2020) 100007.
[19] F. Yan, L. Xu, Y. Wang, S. Park, S.M. Sarathy, S.H. Chung, On the opposing effects of methanol and ethanol addition on PAH and soot formation in ethylene counterflow diffusion flames, Combust. Flame 202 (2019) 228–242.
[20] L. Xu, F. Yan, M. Zhou, Y. Wang, S.H. Chung, Experimental and soot modeling studies of ethylene counterflow diffusion flames: non-monotonic influence of the oxidizer composition on soot formation, Combust. Flame 197 (2018) 304–318.
[21] Y. Wang, S.H. Chung, Effect of strain rate on sooting limits in counterflow diffusion flames of gaseous hydrocarbon fuels: sooting temperature index and sooting sensitivity index, Combust. Flame 161 (2014) 1224–1234.
[22] H. Wang, D.X. Du, C.J. Sung, C.K. Law, Experiments and numerical simulation on soot formation in opposed-jet ethylene diffusion flames, Proc. Combust. Inst. 26 (1996) 2359–2368.
[23] A. D'Anna, M. Commodo, M. Sirignano, P. Minutolo, R. Pagliara, Particle formation in opposed-flow diffusion flames of ethylene: an experimental and numerical study, Proc. Combust. Inst. 32 (2009) 793–801.
[24] M. Sirignano, A. Collina, M. Commodo, P. Minutolo, A. D'Anna, Detection of aromatic hydrocarbons and incipient particles in an opposed-flow flame of ethylene by spectral and time-resolved laser induced emission spectroscopy, Combust. Flame 159 (2012) 1663–1669.
[25] M. Sirignano, J. Kent, A. D'Anna, Further experimental and modelling evidences of soot fragmentation in flames, Proc. Combust. Inst. 35 (2015) 1779–1786.
[26] A. D'Anna, Combustion-formed nanoparticles, Proc. Combust. Inst. 32 (2009) 593–613.
[27] H. Bockhorn, A. D'Anna, A.F. Sarofim, H. Wang, Combustion Generated Fine Carbonaceous Particles, Gordon and Breach, 1994.
[28] J. Xiao, E. Austin, W.L. Roberts, Relative polycyclic aromatic hydrocarbon concentrations in unsteady counterflow diffusion flames, Combust. Sci. Technol. 177 (2005) 691–713.
[29] D. Veynante, L. Vervisch, Turbulent combustion modeling, Prog. Energy Combust. Sci. 28 (2002) 193–266.
[30] H. Guo, Z. Gu, K.A. Thomson, G.J. Smallwood, F.F. Baksh, Soot formation in a laminar ethylene/air diffusion flame at pressures from 1 to 8 atm, Proc. Combust. Inst. 34 (2013) 1795–1802.
[31] P. Vannorsdall, X. Xue, K. Twarog, C.-J. Sung, Sooting propensities of FACE gasolines in counterflow nonpremixed flames, Energy Fuels 35 (2021) 16101–16114.
[32] E. Quadarella, J. Guo, A. Cuoci, H.G. Im, Flame-controlling continuation method for extinction of counterflow sooting flames with detailed chemistry, aiaa scitech forum (2022) 2252.
[33] R.L. Axelbalim, W.L. Flower, C.K. Law, Dilution and temperature effects of inert addition on soot formation in counterflow diffusion flames, Combust. Sci. Technol. 61 (1988) 51–73.
[34] J.H. Kent, H.Gg. Wagner, Temperature and fuel effects in sooting diffusion flames, Proc. Combust. Inst. 20 (1985) 1007–1015.
[35] I. Glassman, P. Yaccarino, The temperature effect in sooting diffusion flames, Proc. Combust. Inst. 18 (1981) 1175–1183.
[36] K.P. Schug, Y. Manheimer-Timnat, P. Yaccarino, I. Glassman, Sooting behavior of gaseous hydrocarbon diffusion flames and the influence of additives, Combust. Sci. Technol. 22 (1980) 235–250.
[37] B.G. Sarnacki, H.K. Chelliah, Sooting limits of non-premixed counterflow ethylene/oxygen/inert flames using LII: effects of flow strain rate and pressure (up to 30 atm), Combust. Flame 195 (2018) 267–281.
[38] A.L. Randolph, C.K. Law, Time-resolved gasification and sooting characteristics of droplets of alcohol/oil blends and water/oil emulsions, Proc. Combust. Inst. 21 (1988) 1125–1131.
[39] M. Salamanca, M. Sirignano, A. D'Anna, Particulate formation in premixed and counter-flow diffusion ethylene/ethanol flames, Energy Fuels 26 (2012) 6144–6152.
[40] M. Salamanca, M. Sirignano, M. Commodo, P. Minutolo, A. D'Anna, The effect of ethanol on the particle size distributions in ethylene premixed flames, Exp. Therm. Fluid. Sci. 43 (2012) 71–75.
[41] M. Conturso, M. Sirignano, A. D'Anna, Effect of C9H12 alkylbenzenes on particle formation in diffusion flames: an experimental study, Fuel 191 (2017) 204–211.
[42] M. Sirignano, M. Conturso, A. D'Anna, Effect of furans on particle formation in diffusion flames: an experimental and modeling study, Proc. Combust. Inst. 35 (2015) 525–532.
[43] M. Conturso, M. Sirignano, A. D'Anna, Effect of alkylated aromatics on particle formation in diffusion flames: an experimental study, Exp. Therm. Fluid Sci. 73 (2016) 27–32.
[44] M. Sirignano, D. Bartos, M. Conturso, M. Dunn, A. D'Anna, A.R. Masri, Detection of nanostructures and soot in laminar premixed flames, Combust. Flame 176 (2017) 299–308.
[45] P. Minutolo, M. Commodo, A. D'Anna, Optical properties of incipient soot, Proc. Combust. Inst. 39 (2023) 1129–1138.
[46] A. D'Anna, Combustion-formed nanoparticles, Proc. Combust. Inst. 32 (2009) 593–613.
[47] U. Niemann, K. Seshadri, F.A. Williams, Accuracies of laminar counterflow flame experiments, Combust. Flame 162 (2015) 1540–1549.
[48] K. Seshadri, F.A. Williams, Laminar flow between parallel plates with injection of a reactant at high Reynolds number, Int. J. Heat Mass Transf. 21 (1978) 251–253.
[49] M. Sirignano, M. Salamanca, A. D'Anna, The role of dimethyl ether as substituent to ethylene on particulate formation in premixed and counter-flow diffusion flames, Fuel 126 (2014) 256–262.
[50] U. Niemann, K. Seshadri, F.A. Williams, Accuracies of laminar counterflow flame experiments, Combust. Flame 162 (2015) 1540–1549.
[51] R. Schmitz, F. Ferraro, M. Sirignano, C. Hasse, Numerical and experimental investigations on the particle formation in oxymethylene ethers (OME, n = 2–4)/ethylene premixed flames, Fuel 357 (2024) 129762.
[52] F. Ferraro, C. Russo, R. Schmitz, C. Hasse, M. Sirignano, Experimental and numerical study on the effect of oxymethylene ether-3 (OME3) on soot particle formation, Fuel 286 (2021) 119353.
[53] C.R. Shaddix, Correcting Thermocouple Measurements for Radiation Loss: A Critical Review, Sandia National Labs, 1999.
[54] A. Nobili, A. Cuoci, W. Pejpichestakul, M. Pelucchi, C. Cavallotti, T. Faravelli, Modeling soot particles as stable radicals: a chemical kinetic study on formation

and oxidation. Part I. Soot formation in ethylene laminar premixed and counterflow diffusion flames, Combust. Flame 243 (2022) 112073.
[55] H. Bladh, N.-E. Olofsson, T. Mouton, J. Simonsson, X. Mercier, A. Faccinetto, et al., Probing the smallest soot particles in low-sooting premixed flames using laser-induced incandescence, Proc. Combust. Inst. 35 (2015) 1843–1850.
[56] W. Pejpichestakul, A. Frassoldati, A. Parente, T. Faravelli, Kinetic modeling of soot formation in premixed burner-stabilized stagnation ethylene flames at heavily sooting condition, Fuel 234 (2018) 199–206.
[57] C. Saggese, S. Ferrario, J. Camacho, A. Cuoci, A. Frassoldati, E. Ranzi, et al., Kinetic modeling of particle size distribution of soot in a premixed burner-stabilized stagnation ethylene flame, Combust. Flame 162 (2015) 3356–3369.
[58] A. Nobili, W. Pejpichestakul, M. Pelucchi, A. Cuoci, C. Cavallotti, T. Faravelli, Modeling soot particles as stable radicals: a chemical kinetic study on formation and oxidation. Part II. Soot oxidation in flow reactors and laminar flames, Combust. Flame 243 (2022) 112072.
[59] R.J. Kee, F.M. Rupley, E. Meeks, J.A. Miller, CHEMKIN-III: A FORTRAN Chemical Kinetics Package for the Analysis of Gas-Phase Chemical and Plasma Kinetics, Sandia National Labs, 1996.
[60] A. Cuoci, A. Frassoldati, T. Faravelli, E. Ranzi, OpenSMOKE++: an object-oriented framework for the numerical modeling of reactive systems with detailed kinetic mechanisms, Comput. Phys. Commun. 192 (2015) 237–264.
[61] A. Cuoci, A. Frassoldati, T. Faravelli, E. Ranzi, Formation of soot and nitrogen oxides in unsteady counterflow diffusion flames, Combust. Flame 156 (2009) 2010–2022.
[62] A. Gomez, D.E. Rosner, Thermophoretic effects on particles in counterflow laminar diffusion flames, Combust. Sci. Technol. 89 (1993) 335–362.
[63] W. Pejpichestakul, E. Ranzi, M. Pelucchi, A. Frassoldati, A. Cuoci, A. Parente, et al., Examination of a soot model in premixed laminar flames at fuel-rich conditions, Proc. Combust. Inst. 37 (2019) 1013–1021.
[64] S.S. Sazhin, An approximation for the absorption coefficient of soot in a radiating gas, Fluent Europe Ltd, 1994.
[65] P.B. Taylor, P.J. Foster, Some gray weighting coefficients for CO2–H2O–soot mixtures, Int. J. Heat Mass Transf. 18 (1974) 1331–1332.
[66] T.F. Smith, Z.F. Shen, J.N. Friedman, Evaluation of coefficients for the weighted sum of gray gases model, J. Heat. Transf. 104 (1982) 602–608.
[67] R.J. Hall, Radiative dissipation in planar gas-soot mixtures, J. Quant. Spectrosc. Radiat. Transf. 51 (1994) 635–644.
[68] R.S. Barlow, A.N. Karpetis, J.H. Frank, J-Y. Chen, Scalar profiles and NO formation in laminar opposed-flow partially premixed methane/air flames, Combust. Flame 127 (2001) 2102–2118.
[69] X.L. Zhu, J.P. Gore, A.N. Karpetis, R.S. Barlow, The effects of self-absorption of radiation on an opposed flow partially premixed flame, Combust. Flame 129 (2002) 342–345.
[70] J.H. Frank, R.S. Barlow, C. Lundquist, Radiation and nitric oxide formation in turbulent non-premixed jet flames, Proc. Combust. Inst. 28 (2000) 447–454.
[71] R.S. Barlow, N.S.A. Smith NSA, J-Y. Chen, R.W. Bilger, Nitric oxide formation in dilute hydrogen jet flames: isolation of the effects of radiation and turbulence-chemistry submodels, Combust. Flame 117 (1999) 4–31.
[72] G.B. Ferraris, D. Manca, BzzOde, Comput. Chem. Eng. 22 (1998) 1595–1621.
[73] D. Bartos, M. Sirignano, M.J. Dunn, A. D'Anna, A.R. Masri, Soot inception in laminar coflow diffusion flames, Combust. Flame 205 (2019) 180–192.
[74] J.A. Rundel, C.M. Thomas, P.E. Schrader, K.R. Wilson, K.O. Johansson, R. P. Bambha, et al., Promotion of particle formation by resonance-stabilized radicals during hydrocarbon pyrolysis, Combust. Flame 243 (2022) 111942.